AGU PUBLICATIONS

JGR

Journal of Geophysical Research: Atmospheres

RESEARCH ARTICLE
10.1002/2016JD024822

Key Points:
- Polar-optimized WRF simulates well physical processes creating daily widespread events in Alaska
- SOMs can be a powerful tool in diagnosing physical characteristics leading to extremes
- The SOM technique gives us another method for analyzing changes in future climate extremes

Correspondence to:
J. M. Glisan,
glisanj@iastate.edu

Citation:
Glisan, J. M., W. J. Gutowski Jr., J. J. Cassano, E. N. Cassano, and M. W. Seefeldt (2016), Analysis of WRF extreme daily precipitation over Alaska using self-organizing maps, *J. Geophys. Res. Atmos.*, *121*, 7746–7761, doi:10.1002/2016JD024822.

Received 19 JAN 2016
Accepted 12 JUN 2016
Accepted article online 22 JUN 2016
Published online 9 JUL 2016

Analysis of WRF extreme daily precipitation over Alaska using self-organizing maps

Justin M. Glisan[1], William J. Gutowski Jr.[1], John J. Cassano[2,3], Elizabeth N. Cassano[2], and Mark W. Seefeldt[2]

[1]Department of Geological and Atmospheric Sciences, Iowa State University of Science and Technology, Ames, Iowa, USA, [2]Cooperative Institute for Research in Environmental Sciences, University of Colorado Boulder, Boulder, Colorado, USA, [3]Department of Atmospheric and Oceanic Sciences, University of Colorado Boulder, Boulder, Colorado, United States

Abstract We analyze daily precipitation extremes from simulations of a polar-optimized version of the Weather Research and Forecasting (WRF) model. Simulations cover 19 years and use the Regional Arctic System Model (RASM) domain. We focus on Alaska because of its proximity to the Pacific and Arctic oceans; both provide large moisture fetch inland. Alaska's topography also has important impacts on orographically forced precipitation. We use self-organizing maps (SOMs) to understand circulation characteristics conducive for extreme precipitation events. The SOM algorithm employs an artificial neural network that uses an unsupervised training process, which results in finding general patterns of circulation behavior. The SOM is trained with mean sea level pressure (MSLP) anomalies. Widespread extreme events, defined as at least 25 grid points experiencing 99th percentile precipitation, are examined using SOMs. Widespread extreme days are mapped onto the SOM of MSLP anomalies, indicating circulation patterns. SOMs aid in determining high-frequency nodes, and hence, circulations are conducive to extremes. Multiple circulation patterns are responsible for extreme days, which are differentiated by where extreme events occur in Alaska. Additionally, several meteorological fields are composited for nodes accessed by extreme and nonextreme events to determine specific conditions necessary for a widespread extreme event. Individual and adjacent node composites produce more physically reasonable circulations as opposed to composites of all extremes, which include multiple synoptic regimes. Temporal evolution of extreme events is also traced through SOM space. Thus, this analysis lays the groundwork for diagnosing differences in atmospheric circulations and their associated widespread, extreme precipitation events.

1. Introduction

Recent studies over the Arctic have shown that regional climate models can produce physically credible simulations of precipitation and temperature extremes [e.g., *Glisan et al.*, 2013; *Eden et al.*, 2014; *Glisan and Gutowski*, 2014a, 2014b; *Wong et al.*, 2014]. While different mechanisms can be responsible for extreme events in different seasons (e.g., convection in summer and synoptic processes in winter), the resolved atmospheric circulations conducive to extreme events are well modeled. The consequences of these extreme events have been shown to have a broad range of negative and long-lasting impacts on the physical environment and society inhabiting these locations, especially the Arctic [*Intergovernmental Panel on Climate Change*, 2014]. Understanding the behavior of contemporary extremes and their associated physical mechanisms is very important with the projected substantial warming across the high latitudes [*Larsen et al.*, 2014]. Additionally, the extremes are projected to increase in occurrence and severity in the future climate [*Collins et al.*, 2013].

In studying weather extremes, an important goal is understanding how large-scale circulations produce conditions favorable for extreme events. This can be time consuming for studies comprising many years as the number of event occurrences multiplies. To reduce the data volume and simplify the process of isolating circulation features conducive to extremes, an analysis method known as self-organizing maps (SOMs) can yield the characteristics of a region's synoptic climatology. *Kohonen* [2001] originally developed the SOM algorithm as a visualization mechanism for higher-dimensional data sets. Studies by several, including *Cavazos* [1999, 2000], *Hewitson and Crane* [2002], *Gutowski et al.* [2004], *E. N. Cassano et al.* [2006], *J. J. Cassano et al.* [2006], and *Cassano et al.* [2007] brought the SOM technique into meteorological and climatological research.

The study of extreme events often involves their spatial and temporal behavior in a region. SOMs have shown a capability to distinguish such behaviors and to segregate a range of spatially unique circulation patterns

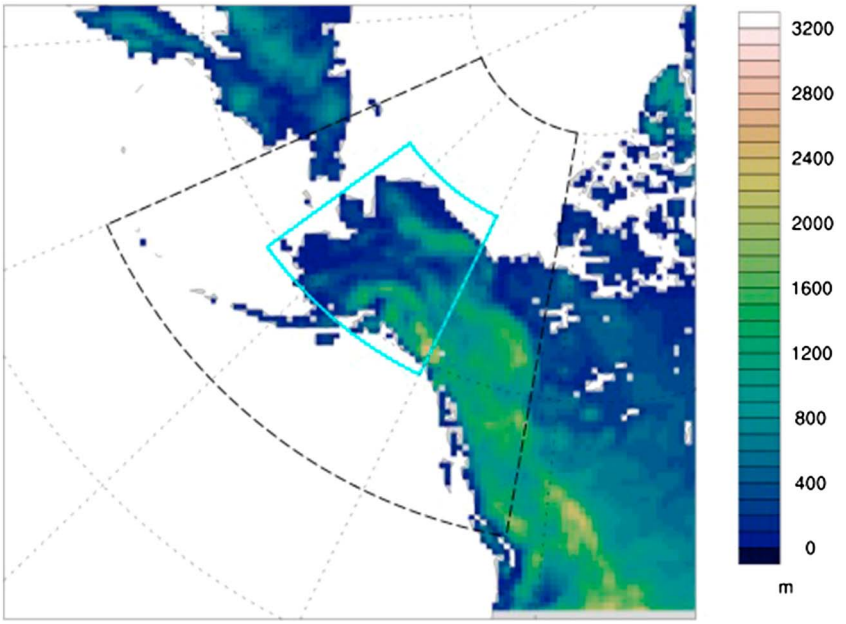

Figure 1. Contoured topography (m) for the Alaska analysis region (light blue line) and larger SOM training region (dashed blue line).

[*E. N. Cassano et al.*, 2006]. This segregation is helpful in distinguishing similar circulation configurations, which appear as adjacent circulation maps in the SOM array. Thus, we can distinguish important differences between similar circulation features present during extreme events.

There are numerous recent studies using SOMs to analyze meteorological variables, including temperature, wind, and precipitation extremes, in the middle and high latitudes. However, SOM studies of extreme precipitation events in the Arctic are not as numerous as those of temperature extremes. *Sheridan and Lee* [2011] reviewed analyses employing SOMs for climatological studies, some of which concentrate on the Arctic and Antarctic. Among these, *E. N. Cassano et al.* [2006] investigated the connection between 2 m temperature and 10 m wind extremes to synoptic circulations in northern Alaska. *Heikkilä and Sorteberg* [2012] used clustering to study the relationship between precipitation and sea level pressure circulations in the cold season across Norway. Precipitation-based SOM studies outside of the high latitudes include wintertime extreme precipitation events over the Balkan Peninsula [*Cavazos*, 2000] and the relationship between circulation and extreme precipitation in northwestern Mexico and southeastern Texas [*Cavazos*, 1999].

This paper focuses on precipitation extremes governed by synoptic weather for winter (December-January-February: DJF) and summer (June-July-August: JJA) over Alaska (Figure 1) from 1992 to 2007. We are interested in Alaska as an Arctic analysis region because of its proximity to the Arctic and Pacific oceans, both of which can supply a large moisture fetch for inland precipitation. The topography of Alaska can also have an important impact on precipitation [*Glisan et al.*, 2013; *Glisan and Gutowski*, 2014a, 2014b]. Additionally, the interaction between semipermanent pressure systems, such as the Beaufort High and Aleutian Low, may play a role in the development and maintenance of transient circulation features that produce widespread precipitation events. In *Glisan and Gutowski* [2014a, 2014b], we used simple composites, to examine widespread extremes. In this paper, we use SOMs to differentiate between particular types of extreme events occurring in different spatial regions.

2. Model, Simulations, and Data

We use a simulation produced by a polar-optimized version of the Advanced Weather Research and Forecasting model (ARW-WRF) [*Skamarock et al.*, 2008] on the 50 km pan-Arctic domain developed for the Regional Arctic System Model (RASM) [*Maslowski et al.*, 2013; J. J. Cassano et al., Atmospheric climate of the regional Arctic system model (RASM), *Journal of Climate*, in review, 2016]. Initial and lateral boundary conditions were produced from two data sets. The first data set is the European Centre for Medium-range Weather Forecasting (ECMWF) ERA-Interim (EI) Reanalysis [*Dee et al.*, 2011]. The EI has been shown to perform well

Table 1. WRF Model Set Up and Parameterization Choices

	Model Set Up
WRF version	3.2
Horizontal grid spacing	50 km
Horizontal grid points	275 *x* grid points × 205 *y* grid points
Number of vertical levels/model top	40/50 mb
Time step	WRF: 2.5 min
Initial and lateral BCs	ERA-I [*Dee et al*., 2011] and NSIDC [*Comiso*, 2008]
Spectral nudging	Variables: temperature, wind, and geopotential heights; nudging wave number: 2 (WRF *x* direction) and 2 (WRF *y* direction); nudging strength: linearly ramped up from 0 at level 20 to 0.0003 s^{-1} at level 10; and nudging depth: Applied to top 20 model levels, with full strength in top 10 model levels.
	Parameterization Choices
Longwave radiation	RRTMG Rapid Radiative Transfer Model (RRTM) for Global Climate Models (GCMS; RRTMG) [*Iacono et al*., 2008]
Shortwave radiation	RRTMG [*Iacono et al*., 2008]
Radiation time step	10 min
Surface layer	Eta Similarity Scheme [*Janjic*, 2002]
Boundary layer	MYJ [*Janjic*, 1994]
Cloud microphysics	Goddard [*Tao et al*., 1989]
Convective parameterization	RH-dependent Additional Perturbation to option 1 for the Kain-Fritsch Scheme [*Kain*, 2004]

across the Arctic [*Lindsay et al*., 2014]. For prescribed sea ice, we use Bootstrap Sea Ice Concentrations [*Comiso*, 2008] from the National Snow and Ice Data Center (NSIDC). The simulation was run continuously, rather than as a series of short forecasts pieced together. Table 1 summarizes many parameterizations and features of the WRF version we used for simulation [*Cassano et al*., 2011, 2015]

We concentrate our analysis on two seasons: winter (December-January-February) and summer (June-July-August) from 1992 to 2007; the simulation covered 1989–2007, but we exclude the first 3 years for model spin-up. We have used the RASM domain in the past [*Glisan et al*., 2013] because it is large enough to encompass the synoptic-scale circulations that directly influence Alaska precipitation. Additionally, the domain encompasses important transport and interoceanic processes.

For observations, we use the National Climate Data Center's (NCDC) Global Summary of the Day, which includes daily precipitation, 10 m winds, and surface fields. We also use diagnostic fields from the ERA-Interim Reanalysis. We define a precipitation event as precipitation at an observation site or model grid point that exceeds 2.5 mm/day. We chose this threshold since the NCDC stations do not record precipitation below 2.5 mm. For each season and data source, we pool all grid points in the analysis domain together and then extract the top 1% of daily precipitation events to define our extreme events. Additionally, following *Glisan et al*. [2013] and *Glisan and Gutowski* [2014a, 2014b], we define widespread events as covering at least 25 model grid points or 16 NCDC stations.

3. Analysis Methods

3.1. Precipitation Extremes

Our analysis of precipitation extremes uses two diagnostics. The first is frequency versus intensity plots, constructed using normalized histograms; we use the criteria in *Wilks* [1995] to ensure that our bin widths are neither too course nor too fine. To better understand the spatial scale of the extreme precipitation events, we use plots showing the number of precipitation extremes occurring simultaneously on at least N grid points on the same day, so-called simultaneity plots. Since the NCDC stations are not as numerous as the model grid points, we use a normalization procedure to scale the relative importance of observation points versus model grid points. This allows us to account for the different spatial scales resolved by the WRF grid and NCDC station distribution. We determine the scaling factor by dividing the number of grid points in the analysis region by the number of NCDC stations, under an assumption that the stations are roughly evenly distributed [*Glisan and Gutowski*, 2014a, 2014b].

3.2. SOM Training

The SOM technique was developed by *Kohonen* [2001] and has been applied to meteorological and climatological data to evaluate the effects of large-scale circulation on weather patterns, including those present during extreme events. The SOM algorithm is built on a neural network framework that employs an unsupervised

learning method to establish generalized patterns in the data. The algorithm can be considered as a clustering technique that identifies a user-determined number of patterns that span the range of conditions present in the training data. The higher-dimensional input data are simplified by mapping nodes, representing individual circulation maps, onto a two-dimensional surface—the SOM. *Cassano et al*. [2015] provides a detailed explanation of the training procedure.

The SOM training output is effectively a classification array of patterns, the dimensions of which are user defined. The SOM map array is a discrete depiction of a continuous pattern space occupied by the diagnostic field examined. The "self-organizing" aspect of the algorithm comes from the degree to which the input maps organize themselves, through the training procedure.

For our SOM training, we used a domain much larger than our analysis region (Figure 1); this allows for all relevant circulation patterns to be included in the SOM array. The training procedure is well documented by others [e.g., *Hewitson and Crane*, 2002; *Gutowski et al*., 2004; *E. N. Cassano et al*., 2006, 2015].

We train the SOM using daily mean sea level pressure (MSLP) anomalies from the combined WRF and EI fields. We calculate the MSLP anomalies by subtracting each day's region-averaged MSLP from each grid point's value. We use the MSLP anomalies because we want to focus on gradient of MSLP, indicating circulation patterns, and not have fluctuations in overall atmospheric mass in the region during the season influencing the SOM patterns. We also exclude MSLP values at locations above 500 m because differences between EI and WRF in computing MSLP over regions of high and/or complex terrain could produce spurious results.

A benefit of the SOM mapping is that nodes with similar circulation patterns are placed near each other (Figure 2). However, the nodes are not necessarily evenly distributed throughout the pattern space depicted by the SOM; for example, nodes in the top left corner may have much more in common than nodes in the bottom right corner. Further analysis based on the SOM depends partly on knowing how similar adjacent nodes are, which a Sammon map [*Sammon*, 1969] of the SOM array can reveal. A Sammon map is a two-dimensional representation of the higher order data; the distance between nodes and the degree of distortion (e.g., folds and twists) found in the Sammon map is directly related to how the circulations found on each node are related to their neighboring node circulations. A perfectly flat Sammon map would suggest that each node is physically similar to all surrounding nodes; a highly distorted Sammon map would indicate a much more complex SOM and hence more abrupt transitions of circulation patterns across the SOM array. Such a Sammon map could pose interpretation difficulties when analyzing the temporal evolution of an extreme event through SOM space (the SOM array).

3.3. SOM Frequency Analysis

Once we choose the appropriate SOM array for each season, we produce two sets of plots for both observed and simulated precipitation. Specifically, we map all precipitation events on the SOM from the NCDC observations and WRF output. This process shows climatological frequency and the associated daily MSLP anomalies on each SOM node for the targeted season during 1992–2007 (e.g., Figures 5a and 5b for DJF). The other is the frequency of MSLP anomalies in the SOM array for the dates of widespread extreme events (e.g., Figures 5c and 5d). The location of highly accessed nodes (or clusters of nodes) shows the circulation patterns present during extreme events. Moreover, segregating specific events in SOM space will help distinguish geographical and physical mechanism differences between extreme events. These frequency distributions will also allow us to trace the evolution of extreme events through SOM space, thus indicating the evolution of their underlying physical mechanisms.

3.4. Composites

We composite several ERA-Interim and WRF fields for both extreme and nonextreme events on high-frequency nodes. We choose different high-frequency nodes, since the widespread extremes are occurring at different spatial locations. These composites allow us to understand what yields an extreme event compared to a typical precipitation event with a similar MSLP anomaly. This is especially evident in JJA, where mesoscale circulations can be more significant than larger scale circulations. By comparing composites for events occurring at different SOM locations, we can better understand the background mechanisms present, as the MSLP anomaly will be the same for all events on the node.

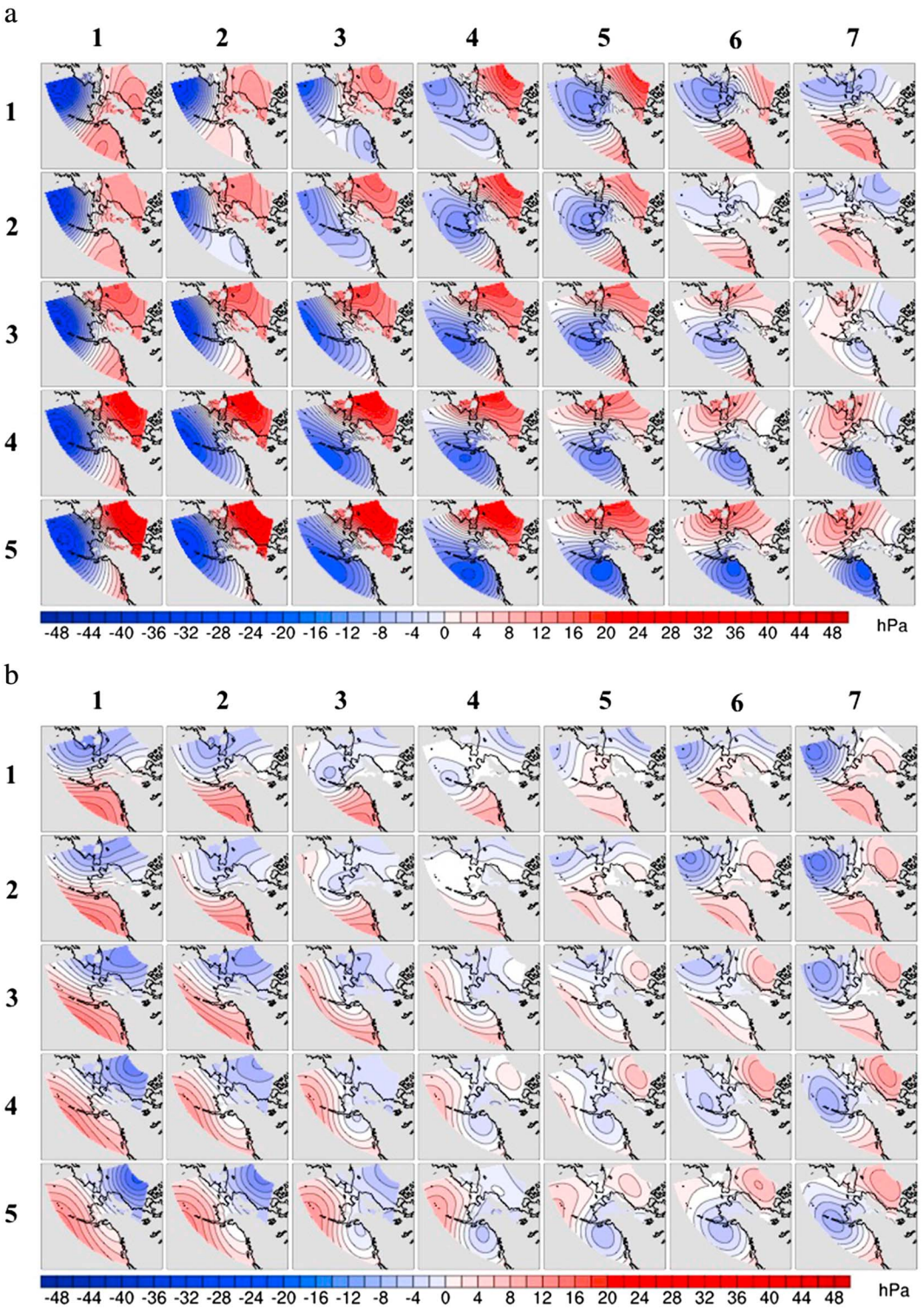

Figure 2. (a) The 7 × 5 SLP anomaly Alaska domain SOM for DJF. Areas in gray represent location above 500 m that have been removed prior to training. Each node represents a dominant synoptic circulation affecting the domain. (b) The 7 × 5 SLP anomaly Alaska domain SOM for JJA. Areas in gray represent location above 500 m that have been removed prior to training. Each node represents a dominant synoptic circulation affecting the domain.

3.5. Temporal Evolution

Using the SOM and our knowledge of the extreme days, we can trace the evolution of an extreme event before and after its day of occurrence. Not only can we glean information such as strengthening or persistence of a transient pressure system, we can also determine whether there exists a specific flow regime evolution that produces a widespread extreme in a certain location in physical space.

To examine temporal evolution, we construct centroids of the event occurrence frequencies in the SOM array for 5 days before and after the extreme event. A centroid here is the frequency-weighted average location in SOM space for the feature tracked (for example, Figure 9a). We calculate an average location and standard deviation to create the centroid; this centroid calculation is performed for each day, allowing us to track the temporal movement through the SOM for the event. We do this for the two highest frequency extreme event nodes for DJF and JJA, as well as for those nodes' climatology. We are interested in how extreme events accessing a high-frequency node evolve through SOM space and how this behavior differs from the climatological evolution.

Centroids in our figures are scaled using the standard deviation of the input frequency distribution; bigger (smaller) centroids indicate a higher (lower) amount of frequency spread within SOM space. For example, smaller centroids indicate frequently accessed nodes are closer together and thus more alike in terms of circulation character. We then plot the centroids on their associated Sammon maps, which highlight how the extreme event evolves through time. The Sammon maps for our SOMs are relatively flat and thus appropriate for temporal analysis; the nodes in the SOMs are physically similar to their immediate neighbors. Centroids for days before (after) an extreme event are shaded from a light to dark gradient of blue (red), with days closer to the event having a darker color.

4. Results

4.1. Precipitation Frequency Versus Intensity

Daily frequency versus intensity plots are shown for DJF (Figure 3a) and JJA (Figure 3b) from the 16 year WRF simulation and NCDC observations. For both seasons, we find that the model is simulating well lower intensity precipitation events. The model shows less agreement with the observations for higher intensity events; this behavior is largely the same as found in Arctic simulations analyzed by *Glisan and Gutowski* [2014a, 2014b]. We have also marked the 95th and 99th percentiles for WRF and NCDC precipitation. In DJF, the model performs well up to the 95th percentile but then has difficulty simulating the highest intensity events. In JJA, the WRF and NCDC percentiles agree well.

Figure 4 shows the simultaneity plots of WRF versus NCDC observations for events above the 99th percentile. The figure shows that for both seasons, the observed and simulated spatial scales of extreme daily precipitation events are largely the same. We also find the DJF widespread extremes cover a larger number of grid points than in JJA. This suggests the DJF extremes are governed by synoptic dynamics, while the JJA extremes are governed by mesoscale processes.

4.2. SOM Frequency Distributions

4.2.1. DJF

Figure 5 shows frequency plots for DJF precipitation climatology in the ERA-Interim (Figure 5a) and the WRF simulation (Figure 5b) MSLP fields. Although the frequency distributions are fairly even, there are some differences between the reanalysis and WRF frequencies. It is important to remember that we create the frequency plots using precipitation events from NCDC; the corresponding circulation fields for the days in which the precipitation events occur (e.g., MSLP) are from the EI reanalysis, since NCDC cannot supply this information.

The three highest frequency ERA-Interim nodes are located in the top and bottom left corners; the general circulation configuration is that of a low pressure in the Bering Sea and high pressure over the Arctic basin. Higher frequency ERA-Interim nodes are concentrated on the top right corner of the SOM. While a large area of higher frequency WRF nodes are found in the bottom right of the SOM, the two highest frequency nodes are located in the top left, in agreement with the ERA-Interim.

There is better agreement when comparing the DJF days with widespread extremes in ERA-Interim (Figure 5c) and WRF (Figure 5d). In winter, we find two locations in SOM space that are accessed frequently by both the

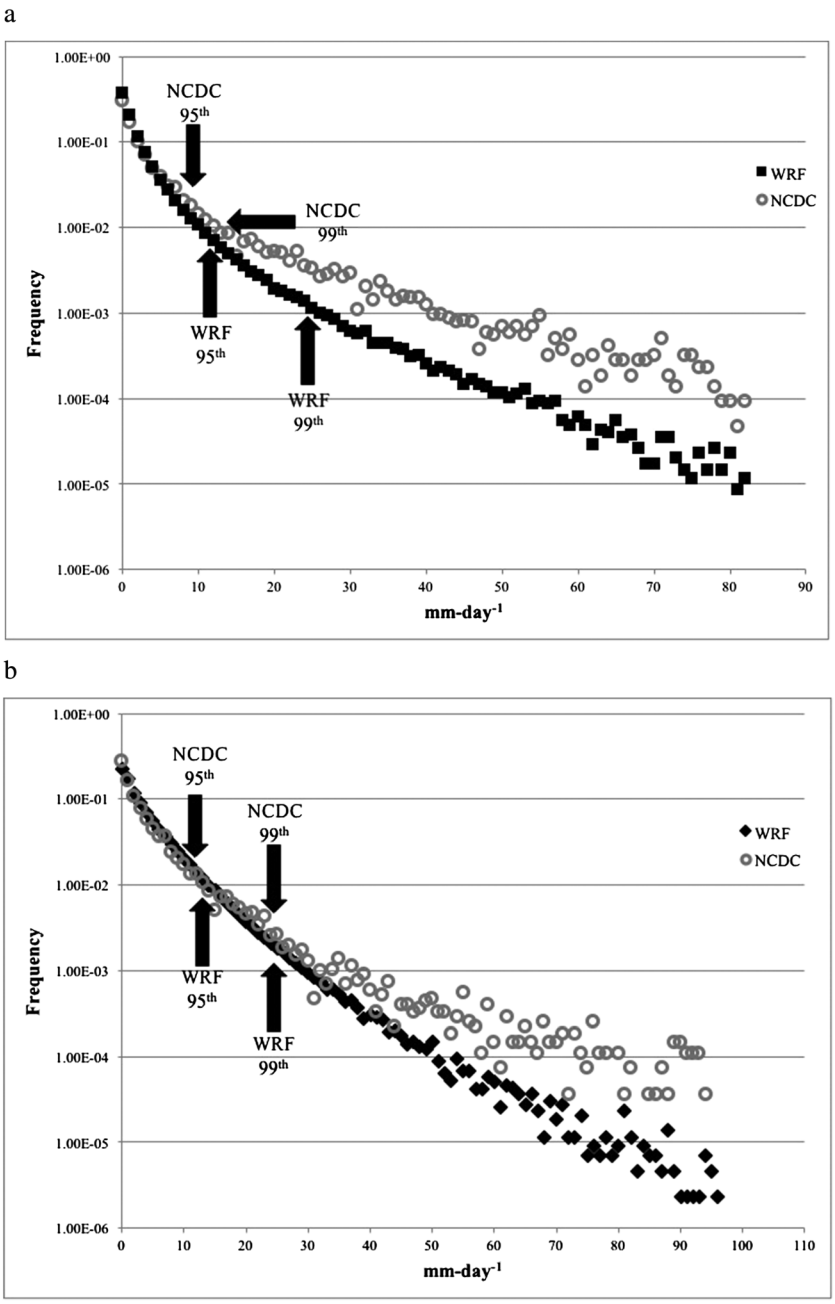

Figure 3. (a) Frequency versus intensity distribution of WRF and NCDC station observations for Alaska in DJF. Black arrows mark the 95th and 99th percentiles for WRF and NCDC. (b) Frequency versus intensity distribution of WRF and NCDC station observations for Alaska in JJA. Black arrows mark the 95th and 99th percentiles for WRF and NCDC.

model and observations during extreme precipitation events, suggesting that two distinct circulations are producing widespread extremes in our analysis region. The first region of interest concentrates on node (1,1), while the second region is found at the opposite side of the SOM array, specifically nodes (6,1) and (7,1) (Figure 2a). For the high-frequency nodes, node (1,1) has a strong low-pressure system in the North Pacific with an area of high pressure over the eastern portion of the analysis domain. Consistent with this circulation configuration, the widespread events occur along the western coast of Alaska. For the second region of interest, the low pressure is located in the Bering Sea. The region of high pressure is also shifted farther south and east of its position in node (1,1). As a result, the widespread precipitation events occur farther inland. Most precipitation events accessing these nodes are located in the Chugach and Wrangell mountain ranges of

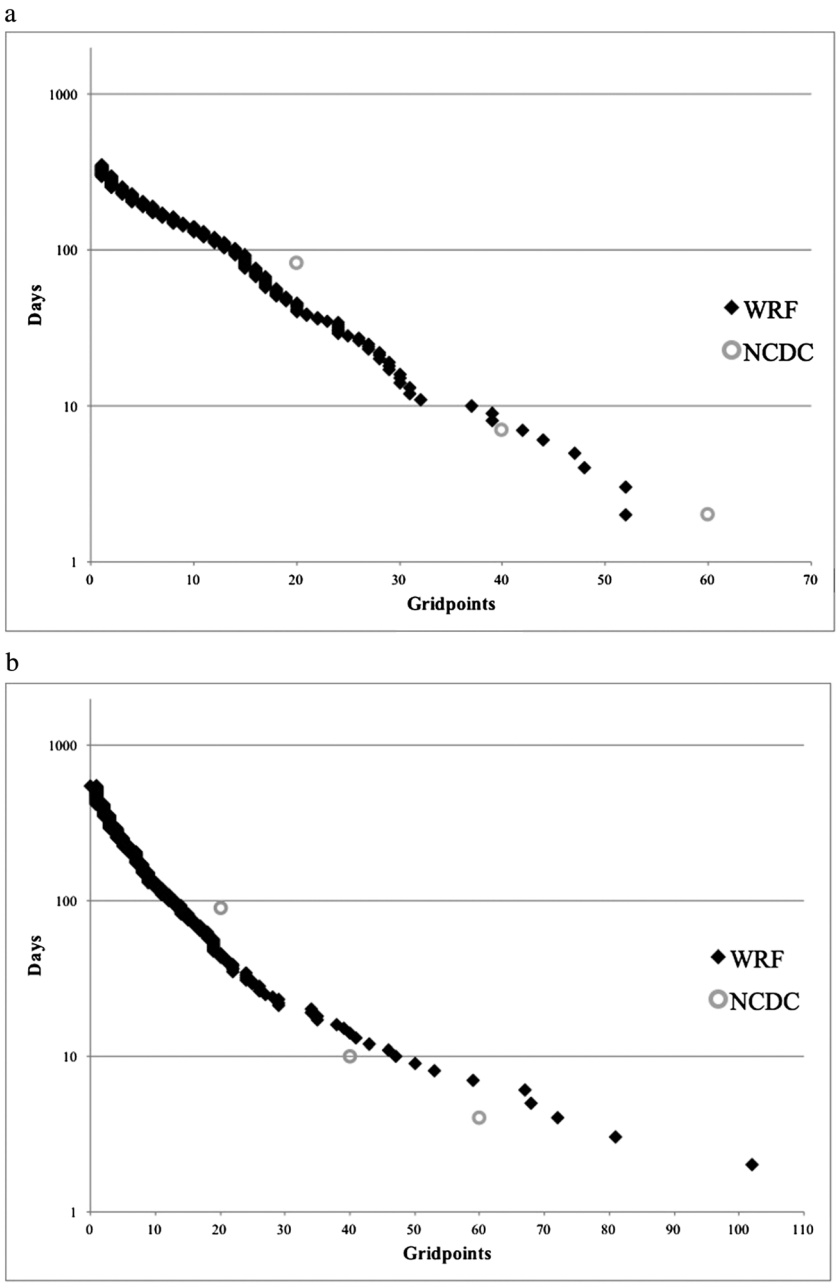

Figure 4. (a) Number of days at least N grid points with precipitation exceeding the 99th percentile in WRF and NCDC station observations for Alaska in DJF. One NCDC station represents 21 grid points. (b) Number of days at least N grid points with precipitation exceeding the 99th percentile in WRF and NCDC station observations for Alaska in JJA. One NCDC station represents 21 grid points.

southeastern Alaska. Since this is a region of high topography, the location of the extremes suggests significant orographic precipitation.

4.2.2. JJA

In the summer season both climatological and extreme frequencies are more dispersed among the nodes than in winter (Figure 6). This behavior may be linked to the smaller variability of circulation patterns between SOM nodes. The reanalysis climatology favors a surface low near the Aleutian Islands and high pressure over Alaska, whereas WRF climatology favors a surface low in the Arctic basin. The distinguishing difference between these regions of SOM space is the location of the low pressure center, which is the dominant feature.

Figure 5. Full Alaska DJF SOM Frequencies for (a) ERA-Interim climatology, (b) WRF climatology, (c) ERA-Interim 99th widespread extremes, and (d) WRF 99th widespread extremes. The ERA-Interim climatology (widespread extremes) plot is produced from MSLP anomaly frequencies for days corresponding to NCDC observed climatological (extremes) events. Cooler (warmer) coloring represents lower (higher) frequency occurrences.

The observed extremes are dispersed across SOM space with two regions of high-frequency nodes in the upper left and lower right quadrants. Simulated widespread extremes in JJA are less dispersed across the SOM and access nodes in the top left quadrant at a higher frequency than any other region of the SOM and thus show some agreement with the observational results. The node circulation patterns for the high-frequency nodes favor a range of low-pressure locations from the Arctic basin into Siberia. An area of weak high pressure over the Gulf of Alaska and inland is consistent across the high-frequency nodes.

In summer, there appears to be a connection to the behavior we are observing and the weaker gradient, subsynoptic scale circulations typically seen in the warm season. The simulated extremes show some agreement with the observations, especially on the left side of SOM space. The observed extreme events also favor a second region on the right side of SOM space, namely, node (7,1) and bottom right quadrant nodes. The circulations associated with these nodes have more distinct centers of high and low pressure relative to the rest of the SOM nodes, with the high located over the Arctic basin and dominant low near the Aleutian Islands. When this configuration is present, we find moisture fetch off of the Gulf of Alaska into the southeastern coastal mountains of the analysis region, producing orographically forced precipitation.

The simulated widespread extremes in summer are accessing nodes on the far left column of the SOM; nodes (1,1) and (1,3) are among the highest frequency nodes within a cluster of higher frequency nodes in the upper left quadrant. While there is a spread in SOM space among the WRF-accessed nodes, the circulations being accessed have a consistent pattern; a low pressure system located north to northwest of Alaska and high pressure over the Gulf of Alaska and inland. This configuration suggests that the low is advecting

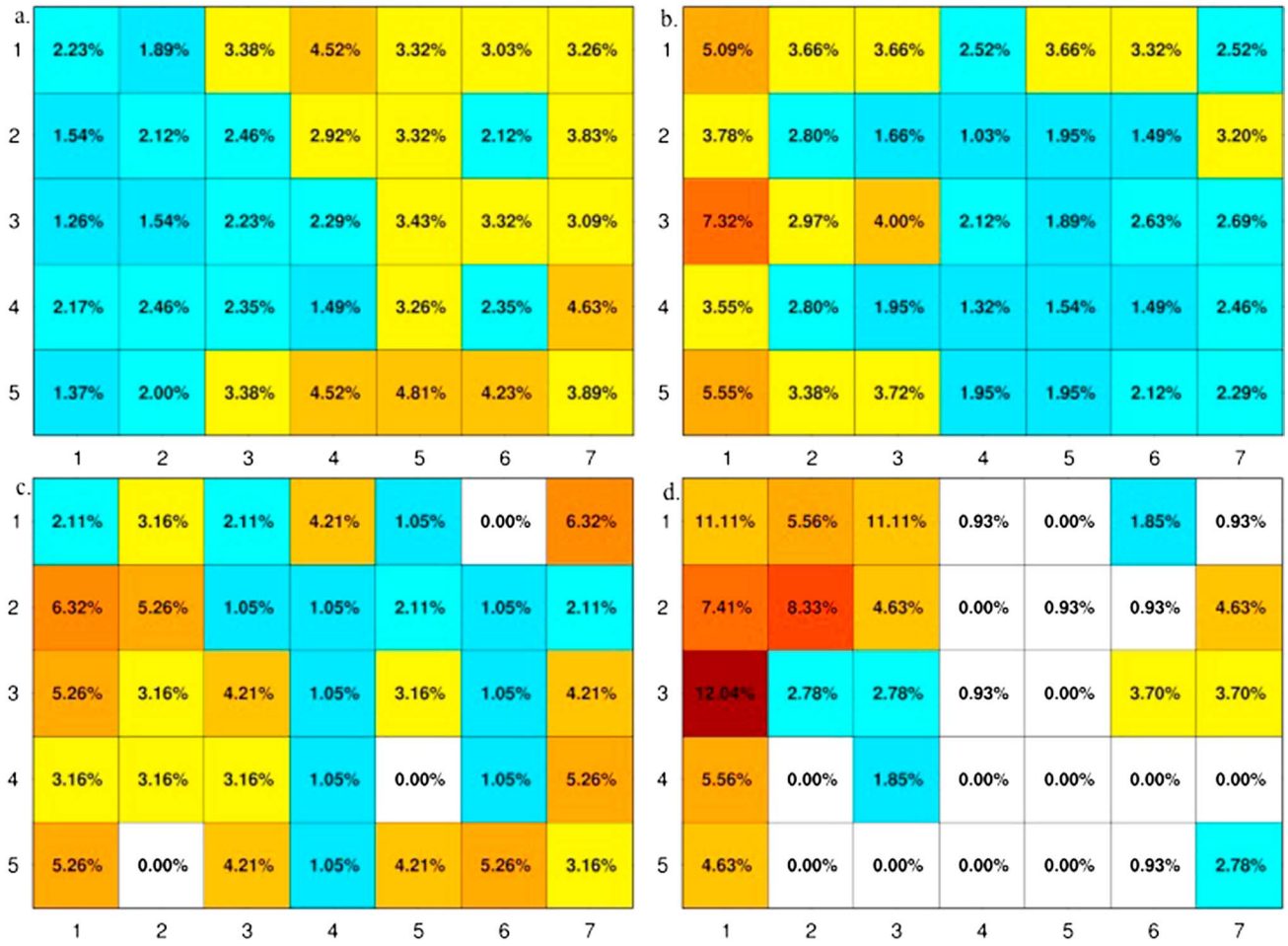

Figure 6. Full Alaska JJA SOM Frequencies for (a) ERA-Interim climatology, (b) WRF climatology, (c) ERA-Interim 99th widespread extremes, and (d) WRF 99th widespread extremes. The ERA-Interim climatology (widespread extremes) plot is produced from MSLP anomaly frequencies for days corresponding to NCDC observed climatological (extremes) events. Cooler (warmer) coloring represents lower (higher) frequency occurrences.

relatively warm, moist air off of the Pacific into the eastern and east-central portions of Alaska. The spatial location of the extreme events confirms this.

As mentioned above, WRF is missing events that are being observed in the bottom right of SOM space. We believe the model is having difficulty simulating these extremes because of the difference in topography between the real world and WRF. In the part of Alaska where these extremes events are observed, the topography varies by 2000 m over less than 20 km. The model cannot resolve such rapidly changing elevation. Thus, smoothed model topography does not provide the necessary barrier forcing to produce real world extremes.

Whereas the DJF SOM segregates specific extreme events in terms of geographic location, the JJA SOM does less so, especially for nodes in the upper left quadrant of SOM space. With mesoscale processes occurring more in the warm season and areas of high topography excluded from the training data, MSLP may be less useful for distinguishing extreme precipitation events in JJA.

4.3. Composite Fields

For winter, we have created both ERA-Interim and WRF composites for node (5,2), though we do not show ERA-Interim for conciseness. We find that on the day of widespread extreme occurrence there is inland moisture fetch into the extreme event region (Figure 7); we see similar behavior for node (1,5), which is not shown. Both nodes show a similar dominant low/weaker high pressure couplet over the analysis region, with the low off the coast of Alaska and the high in the Arctic basin. When we difference the composites for extreme

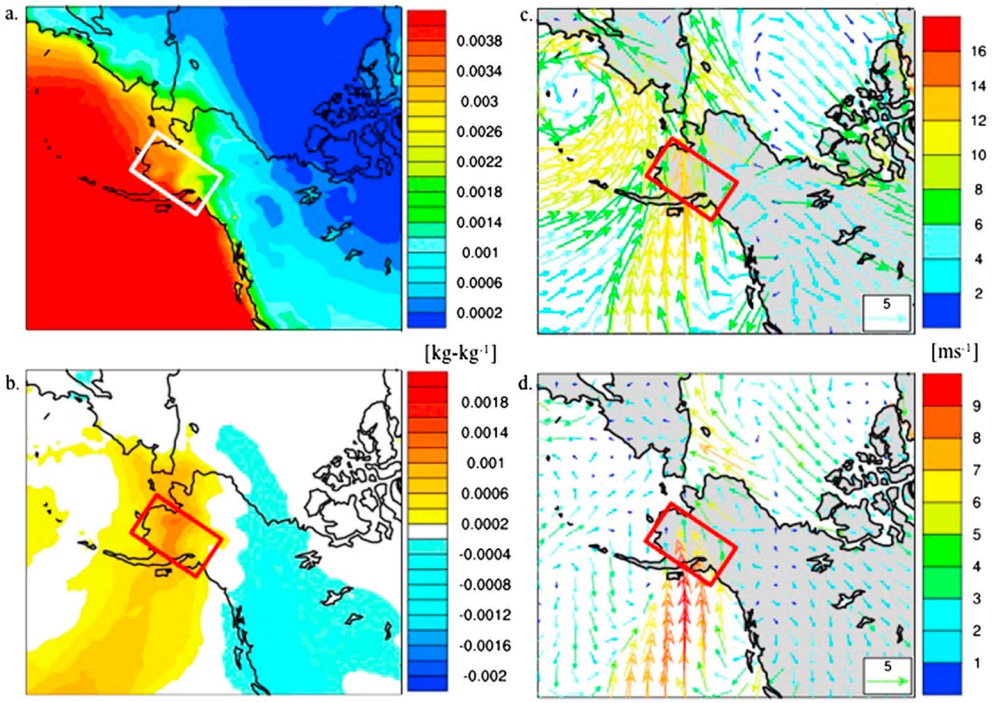

Figure 7. Composites of WRF (a) 2 m specific humidity and (b) 10 m wind vectors on the extreme event days occurring on node (5,2) in DJF. Anomalies of (c) 2 m specific humidity and (d) 10 m wind vectors calculated by subtracting nonextreme events composite from the extreme events composite. Area of extreme event occurrence outlined by red box.

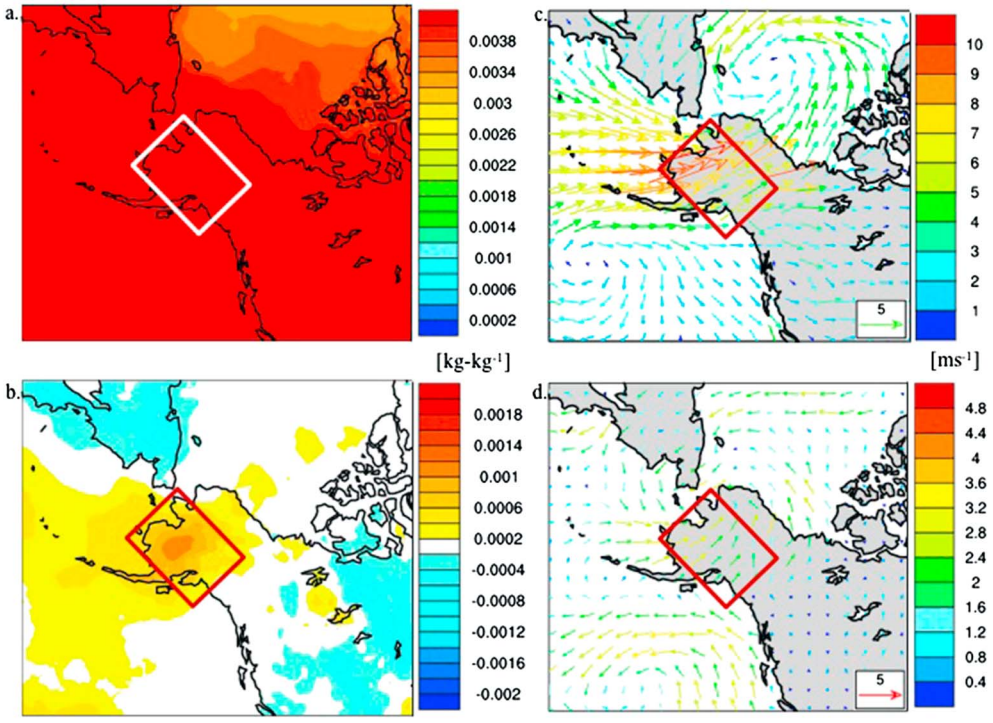

Figure 8. Composites of WRF (a) 2 m specific humidity and (b) 10 m wind vectors on the extreme event days occurring on node (1,3) in JJA. Anomalies of (c) 2 m specific humidity and (d) 10 m wind vectors calculated by subtracting nonextreme events composite from the extreme events composite. Area of extreme event occurrence outlined by red box.

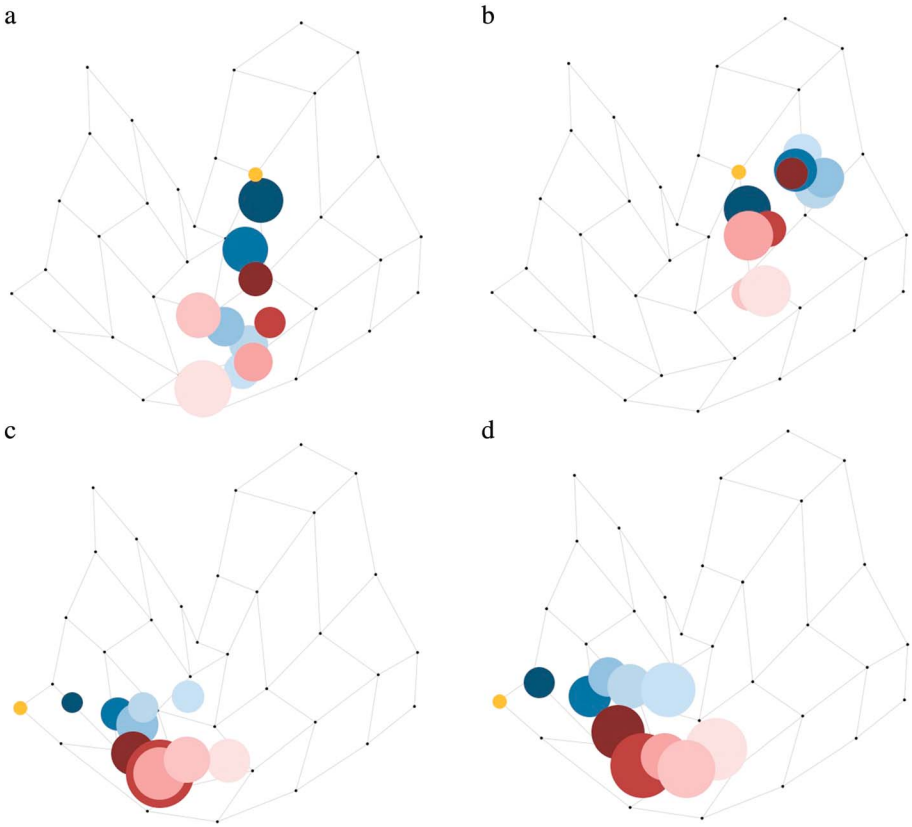

Figure 9. (a) DJF climatology centroids plotted on the Sammon map for reference node (5,2). Blue (red) centroids represent days before (after) the events accessing this node. The color gradient is such that colors become darker the closer to the extreme event node, represented by the yellow circle. (b) DJF extreme centroids plotted on the Sammon map for reference node (5,2). Blue (red) centroids represent days before (after) the events accessing this node. The color gradient is such that colors become darker the closer to the extreme event node, represented by the yellow circle. (c) DJF climatology centroids plotted on the Sammon map for reference node (1,5). Blue (red) centroids represent days before (after) the events accessing this node. The color gradient is such that colors become darker the closer to the extreme event node, represented by the yellow circle. (d) DJF extreme centroids plotted on the Sammon map for reference node (1,5). Blue (red) centroids represent days before (after) the events accessing this node. The color gradient is such that colors become darker the closer to the extreme event node, represented by the yellow circle.

events and nonextreme events accessing these high-frequency nodes, we also find positive anomalies of low-level moisture, 10 m wind vectors and 2 m temperature (not shown), indicating that more moisture was available for the processes creating the extremes. Additionally, a large, positive moisture fetch anomaly into the region of high topography was present; all composite anomalies are colocated with the region in which the widespread precipitation extremes are occurring.

In summer, where segregation within SOM space is less clear-cut, we still find positive anomalies of moisture, temperature (not shown), and fetch (Figure 8). In terms of high access node (1,3) where extremes are occurring in two distinct regions of Alaska, we find that a slight poleward movement of the low pressure (not shown) system near Siberia produces widespread extremes in northern Alaska; an equatorward movement produces extreme events in southern Alaska.

4.4. Temporal Evolution

We analyze the simulated temporal evolution of wintertime extreme and climatology centroids accessing nodes (5,2) and (1,5). As shown in Figure 5d, these nodes are accessed for the simulated widespread extreme events 16.48% and 9.89% of the time, respectively. For WRF climatological evolution, node (5,2) shows a large area of low pressure 3 to 5 days before the extreme events. In the days after the climatological event we find an evolution back to the same circulation state as before the event (Figure 9a). In the days directly before, this area of low pressure consolidates, moves into the Gulf of Alaska, and then retrogresses off the Alaskan west

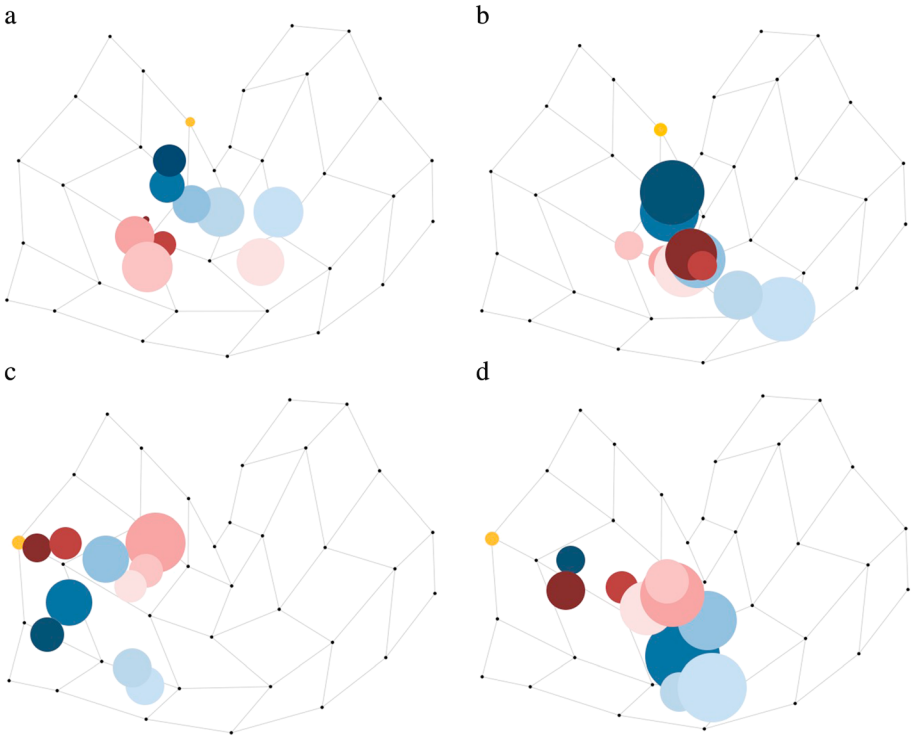

Figure 10. (a) JJA climatology centroids plotted on the Sammon map for reference node (3,1). Blue (red) centroids represent days before (after) the events accessing this node. The color gradient is such that colors become darker the closer to the extreme event node, represented by the yellow circle. (b) JJA extreme centroids plotted on the Sammon map for reference node (3,1). Blue (red) centroids represent days before (after) the events accessing this node. The color gradient is such that colors become darker the closer to the extreme event node, represented by the yellow circle. (c) JJA climatology centroids plotted on the Sammon map for reference node (1,3). Blue (red) centroids represent days before (after) the events accessing this node. The color gradient is such that colors become darker the closer to the extreme event node, represented by the yellow circle. (d) JJA extreme centroids plotted on the Sammon map for reference node (1,3). Blue (red) centroids represent days before (after) the events accessing this node. The color gradient is such that colors become darker the closer to the extreme event node, represented by the yellow circle.

coast. We find some deviation from climatological behavior for the extreme events evolution; the extreme events centroids are larger than the climatology centroids, suggesting more variability in the evolution of the extremes (Figure 9b). The extremes occur with a persistent, weak low-pressure feature in the Gulf of Alaska that eventually retrogresses to the southwest coast of Alaska (Figure 9b). In the days after the event, the area of low pressure moves downstream of the region experiencing the widespread extreme precipitation. Thus, the departure from climatology is most noticeable the farther out in time from the extreme event.

For node (1,5), the climatological and extreme event evolution are similar (Figures 9c and 9d). In the 3 to 5 days prior to the extreme event, a large area of low pressure is present in the Gulf of Alaska, with a large dome of high pressure over the Arctic Basin. This dipole circulation pattern remains consistent in the 2 days before the extreme event, though the low has deepened and retrogressed toward the Aleutian Islands. The combination of cyclonic and anticyclonic flow acts to advect moisture into the central part of Alaska, which is where the widespread precipitation events occur. In the days directly after, the low- and high-pressure features return to the configuration in which they started. The similarity between the climatological and extreme evolution suggests that there must be a distinct mechanism that produces extreme events. Composites of the extreme days show that a slight poleward movement of the low-pressure center occurs on the day of the extreme event. Thus, a slight deviation in the flow configuration may be responsible for producing these widespread extremes.

Nodes (3,1) and (1,3) are the high-frequency nodes of interest in JJA, having 11.11% and 12.04% of access, respectively (Figure 6d). For node (3,1), we find that the climatological (Figure 10a) and extreme event centroids (Figure 10b) have different evolutionary paths through the SOM; extreme event centroids in

the days leading to the high access nodes are much larger; they are accessing a larger region of SOM space. For the days farthest from the extreme node, we find a weak trough retrogress from the center of the domain and transition into a more well defined pressure center, off the southwestern coast of Alaska. In days following the extreme node, the low moves poleward, as high pressure builds into the western portion of the domain.

The differences between the evolution of extreme and climatological events occurring on node 1,3 are more visible, especially for the days leading up to events (Figures 10c and 10d). For the days prior to the climatological events, there is some semblance of a low-pressure retrogressing in the Arctic basin, with a similar propagation of high pressure from the Gulf of Alaska toward the Aleutian Islands (Figure 10c). This evolutionary behavior differs from the extreme events, where we find a weaker pressure gradient (weaker high and low centers), with the low (high) over Alaska (Aleutian Islands; Figure 10d). In the days after the climatological and extreme events, we find similar centroid trajectories (Figure 10d), though the centroids are larger, suggesting a greater range of evolutionary pathways through SOM space to the extreme event. However, the circulation configuration shows a high pressure in the southern part of the domain, with a stronger low-pressure gradient over the Arctic basin and Siberia.

5. Discussion and Conclusions

We have used self-organizing maps to classify circulation patterns conducive for widespread extreme precipitation events in Alaska for winter and summer seasons during 1992–2007. Both seasonal SOMs were trained using combined MSLP anomalies from WRF simulations and ERA-Interim reanalyses. After training, we diagnosed the frequency of occurrence of MSLP patterns for the climatology and for the widespread extreme precipitation events from NCDC and WRF. This is a significant part of the analysis in that climatological synoptic features were identified and then compared to patterns producing extremes. We used a number of analysis techniques, including frequency versus intensity plots, composites of pertinent diagnostic fields, and temporal evolution of high-frequency nodes, to identify important atmospheric features present during widespread extremes.

We defined widespread extreme precipitation events as the top 1% of precipitation events above the 2.5 mm d^{-1} threshold on 25 or more grid points. Frequency versus intensity plots show that the models are simulating well lower intensity events. Only in terms of higher intensity and extreme events do we see a departure from the NCDC observations. We also find that the observed and modeled spatial scales are in good agreement.

We next mapped the NCDC and WRF precipitation climatologies and extremes onto the seasonal SOMs. This technique allows us to compare and analyze circulation features being accessed during extreme events. We compare simulated circulation features to the EI reanalysis MSLP fields. While we do find slight DJF variability in the climatological circulation location, there is good agreement that a low pressure is the dominant circulation mode; the reanalysis (model) low center is found in the Gulf of Alaska (Bering Sea). The observed and simulated winter precipitation extremes show good agreement in terms of their location in SOM space; we found two high frequency clusters, each having a distinct circulation character. Both clusters show a dipole feature, with a high pressure in the east and a deep low pressure in the west. The clusters differ in that the cluster one has the dipole further upstream than cluster two. This change in location produces two distinct extreme locations in Alaska. Cluster one (two) produces extremes on the southwest coast (Gulf coast) of Alaska.

In summer, the observed and simulated climatologies accessed opposite ends of SOM space. However, the widespread extremes from both NCDC and WRF were found to occupy the same leftmost columns of the SOM. The circulation configuration found in this portion of SOM space favors a low pressure over the Arctic, with high pressure over the Pacific. In a departure from DJF, the SOM is having some difficulty differentiating the spatial locations of extreme events on high-frequency nodes in different parts of SOM space. For example, extreme events on node (1,3) are found in different parts of Alaska. This behavior may be connected to the mesoscale dynamics dominating precipitation production in JJA. Specifically, the subgrid processes may affect the skill of the SOM training, especially since topography below 500 m is masked out.

We produced composites of high-frequency nodes for widespread extreme and nonextreme events, for both seasons. The difference plots show that positive anomalies of low-level moisture, temperature, and wind speed were collocated with the regions in which extreme precipitation events were occurring. Even in

situations where extremes are occurring in multiple spatial regions on a high-frequency node (e.g., JJA node (1,3)), the composites highlight the conditions present during extreme precipitation events.

Another capability of the SOM algorithm is the analysis of extreme event time evolution through SOM space. For both seasons, we chose two high-frequency nodes in different parts of SOM space. We then analyzed how the circulation present on the day of the extremes evolved, using a lead/lag time of 5 days.

For DJF, spatial extremes were found in two different parts of Alaska. While the climatological and extremes evolution agreed well in the days immediately prior to, and after, the node is accessed—low pressure near the Gulf of Alaska retrogressing toward the southwest coast of Alaska—we find some degree of disagreement on the peripheries of the lead/lag days. We do find that a near-identical flow configuration is present 3 to 5 days prior, as well as many days out, from the extreme node. This suggests a strong synoptic signal in the temporal evolution. However, in the case of the second spatial extreme location of occurrence there is also a strong high pressure present over the Arctic basin. The combined cyclonic/anticyclonic flows act to advect moisture into central Alaska, where the extreme events accessing this node are found.

Temporal analysis in summer shows less agreement between climatological and extreme evolution in the days after extreme event occurrence. As noted in DJF, a retrogressing cyclone is found in the days leading to the extreme events; the location of the cyclone in the days prior to the event is directly responsible for the spatial location of the widespread precipitation events in Alaska. In general, the centroids are larger than what is found in the DJF trajectories; more of SOM space is being accessed, and hence, a larger variety of circulations are present on the lead up to the extreme events. The behavior seems to be tied to the relaxed gradients and mesoscale-type flows that dominate most summer SOM nodes. These flow characteristics also might lend to the SOM not segregating extreme event locations as well as in DJF, which suggests training on MSLP may not do as well for warm season Alaska

Overall, SOMs do a good job at highlighting how precipitation extremes occurring in specific parts of Alaska correspond to high-frequency nodes in different regions of SOM space. SOMs can be a powerful tool in diagnosing physical characteristics leading to extremes. Specifically, SOMs helped classify the dominant circulation features present during widespread precipitation extremes. This study is a further indication of the SOM's ability to segregate extremes having different spatial locations, as well as dynamic features. Coupled with WRF's ability to simulate well the physical processes creating daily widespread events in Alaska, the SOM technique gives us another method for analyzing changes in future climate extremes.

Acknowledgments

This research was supported by U.S. Department of Energy grant DEFG0207ER64463 and National Science Foundation grant ARC1023369. The authors thank two anonymous reviewers for their comments, which helped improve the manuscript. ERA-Interim data can be accessed via the ECMWF's data repository (http://apps.ecmwf.int/datasets/data/interim-full-daily/levtype=sfc/). The NCDC station observations can be accessed via their website (https://data.noaa.gov/dataset/global-surface-summary-of-the-day-gsod). The simulation results and figures are available from the authors upon request (glisanj@iastate.edu).

References

Cassano, E. N., A. H. Lynch, J. J. Cassano, and M. R. Koslow (2006), Classification of synoptic patterns in the western Arctic associated with extreme events at Barrow, Alaska, USA, *Clim. Res.*, *30*, 83–97.

Cassano, E. N., J. Glisan, J. J. Cassano, W. Gutowski, and M. Seefeldt (2015), Methodology of using the self-ogranizing map algorithm to characterize and analyze temperature extremes in Alaska and Canada, *Clim. Res.*, *62*, 199–219, doi:10.3354/cr01274.

Cassano, J. J., O. Uotila, and A. Lynch (2006), Changes in synoptic weather patterns in the polar regions in the 20th and 21st centuries, Part 1: Arctic, *Int. J. Climatol.*, *26*(8), 1027–1049, doi:10.1002/joc.1306.

Cassano, J. J., P. Uotilla, A. H. Lynch, and E. N. Cassano (2007), Predicted changes in synoptic forcing of net precipitation in large Arctic river basins during the 21st century, *J. Geophys. Res.*, *112*, G04S49, doi:10.1029/2006JG000332.

Cassano, J. J., M. E. Higgins, and M. W. Seefeldt (2011), Performance of the Weather Research and Forecasting (WRF) model for month-long pan-Arctic simulations, *Mon. Weather Rev.*, *139*, 3469–3488, doi:10.1175/MWR-D-10-05065.1.

Cavazos, T. (1999), Large-scale circulation anomalies conducive to extreme precipitation events and derivation of daily rainfall in northeastern Mexico and southeastern Texas, *J. Clim.*, *12*, 1506–1523.

Cavazos, T. (2000), Using self-organizing maps to investigate extreme climate events: An application to wintertime precipitation in the Balkans, *J. Clim.*, *13*, 1718–1732.

Collins, M., et al. (2013), Long-term climate change: Projections, commitments and irreversibility, in *Climate Change 2013: The Physical Science Basis. Contribution of Working Group I to the Fifth Assessment Report of the Intergovernmental Panel on Climate Change*, edited by T. F. Stocker et al., Cambridge Univ. Press, Cambridge, U. K., and New York.

Comiso, J. (2008), *Bootstrap Sea Ice Concentrations from NIMBUS-7 SMMR and DMSP SSM/I, 1989–2007*, Natl. Snow and Ice Data Cent., Boulder, Colo., Digital media.

Dee, D. P., et al (2011), The ERA Interim reanalysis: Configuration and performance of the data assimilation system, *Q. J. R. Meteorol. Soc.*, *137*, 553–597, doi:10.1002/qj.828.

Eden, J. M., M. Widmann, D. Maraun, and M. Vrac (2014), Comparison of GCM- and RCM-simulated precipitation following stochastic postprocessing, *J. Geophys. Res. Atmos.*, *119*, 11,040–11,053, doi:10.1002/2014JD021732.

Glisan, J. M., and W. J. Gutowski Jr. (2014a), WRF summer extreme daily precipitation over the CORDEX Arctic, *J. Geophys. Res. Atmos.*, *119*, 1720–1732, doi:10.1002/2013JD020697.

Glisan, J. M., and W. J. Gutowski Jr. (2014b), WRF winter extreme daily precipitation over the North American CORDEX Arctic, *J. Geophys. Res. Atmos.*, *119*, 10,738–10,748, doi:10.1002/2014JD021676.

Glisan, J. M., W. J. Gutowski Jr., J. J. Cassano, and M. E. Higgins (2013), Effects of spectral nudging in WRF on Arctic temperature and precipitation simulations, *J. Clim.*, *26*, 3985–3999, doi:10.1175/JCLI-D-12-00318.1.

Gutowski, W. J., F. Otieno, R. W. Arritt, E. S. Takle, and Z. Pan (2004), Diagnosis and attribution of a seasonal precipitation deficit in a U.S. regional climate simulation, *J. Hydrometeorol.*, *5*, 230–242, doi:10.1175/1525-7541(2004)005<0230:DAAOAS>2.0.CO;2.

Heikkilä, U., and A. Sorteberg (2012), Characteristics of autumn-winter extreme precipitation on the Norwegian west coast identified by cluster analysis, *Clim. Dyn.*, *39*(3–4), 929–939.

Hewitson, B. C., and R. G. Crane (2002), Self-organizing maps: Applications to synoptic climatology, *Clim. Res.*, *22*, 13–26.

Iacono, M. J., J. S. Delamere, E. J. Mlawer, M. W. Shephard, S. A. Clough, and W. D. Collins (2008), Radiative forcing by long–lived greenhouse gases: Calculations with the AER radiative transfer models, *J. Geophys. Res.*, *113*, D13103, doi:10.1029/2008JD009944.

Intergovernmental Panel on Climate Change (2014), *Climate Change 2014: Impacts, Adaptation, and Vulnerability. Part B: Regional Aspects. Contribution of Working Group II to the Fifth Assessment Report of the Intergovernmental Panel on Climate Change*, edited by V. R. Barros et al., 688 pp., Cambridge Univ. Press, Cambridge, U. K., and New York.

Janjic, Z. I. (1994), The step–mountain eta coordinate model: Further developments of the convection, viscous sublayer, and turbulence closure schemes, *Mon. Weather Rev.*, *122*, 927–945.

Janjic, Z. I. (2002), Nonsingular implementation of the Mellor-Yamada Level 2.5 Scheme in the NCEP Meso model, NCEP Office Note 437, 61 pp.

Kain, J. S. (2004), The Kain–Fritsch convective parameterization: An update, *J. Appl. Meteorol.*, *43*, 170–181.

Kohonen, T. (2001), *Self-Organizing Maps*, Springer, New York.

Larsen, J. N., O. A. Anisimov, A. Constable, A. B. Hollowed, N. Maynard, P. Prestrud, T. D. Prowse, and J. M. R. Stone (2014), Polar regions, in *Climate Change 2014: Impacts, Adaptation, and Vulnerability. Part B: Regional Aspects. Contribution of Working Group II to the Fifth Assessment Report of the Intergovernmental Panel on Climate Change*, edited by V. R. Barros et al., pp. 1567–1612, Cambridge Univ. Press, Cambridge, U. K., and New York.

Lindsay, R., M. Wensnahan, A. Schweiger, and J. Zhang (2014), Evaluation of seven different atmospheric reanalysis products in the Arctic, *J. Clim.*, *27*, 2588–2606, doi:10.1175/JCLI-D-13-00014.1.

Maslowski, W., J. Cassano, W. Gutowski, and D. Lettenmaier (2013), Towards advanced understanding and predictive capability of climate change in the Arctic using a high-resolution regional Arctic climate system model (RACM). DOE Climate Change Prediction Program Meeting. [Available at http://ccpp.llnl.gov/projects/2009/cassano.html?projectSerial=5917&query_id=0&searchpage=index.jsp.]

Sammon, J. W. (1969), A non-linear mapping for data structure analysis, *IEEE Trans. Comput.*, *C-18*, 401–409.

Sheridan, S. C., and C. C. Lee (2011), The self-organizing map in synoptic climatological research, *Prog. Phys. Geogr.*, *35*, 109–119, doi:10.1177/0309133310397582.

Skamarock, W. C., J. B. Klemp, J. Dudhia, D. O. Gill, D. M. Barker, M. Duda, X.-Y. Huang, and J. G. Powers (2008), A description of the Advanced Research WRF version 3, *NCAR Tech. Note NCAR/TN-4751STR*, 113 pp.

Tao, W.–. K., J. Simpson, and M. McCumber (1989), An ice–water saturation adjustment, *Mon. Weather Rev.*, *117*, 231–235.

Wilks, D. S. (1995), *Statistical Methods in the Atmospheric Sciences: An Introduction*, pp. 467, Academic Press, Amsterdam, The Netherlands.

Wong, G., D. Maraun, M. Vrac, M. Widmann, J. M. Eden, and T. Kent (2014), Stochastic model output statistics for bias correcting and downscaling precipitation including extremes, *J. Clim.*, *27*, 6940–6959.